Cavity quantum electrodynamics with quantum dots in microcavities

Bakker, M.P.

Chapter 9

Outlook

In this chapter we start with a discussion on 3 ongoing studies, which are not yet ready for publication in a scientific journal but are still important preliminary results and offer food for thought and discussion: (i) First, we will present photon time correlation measurements that were performed by resonantly probing a coupled QD–cavity system. Clear signatures of bunching and anti-bunching are demonstrated. (ii) Next, we will propose a method to study phonon induced exciton dephasing via an asymmetry in the QD dephasing rate between red and blue cavity detunings in our current cavity QED sample. The challenge lies in distinguishing between these phonon influences and other (voltage dependent) dephasing effects. (iii) Finally, we propose a method to increase the fidelity of quantum operations by using the full polarization degree of freedom in a polarization degenerate microcavity. By tuning the input and output polarizations and using interference of orthogonal light components, the contrast between a coupled and uncoupled QD–cavity system can be dramatically enhanced.

We conclude with a discussion on some of the drawbacks of our current sample ('131018A') that were discovered during the work in this thesis, and discuss improvements for new sample generations.

9.1 Photon correlation measurements

A cavity QED system that is resonantly probed can convert coherent laser light into non-classical states of light that follows super-Poissonian statistics (bunched photons) or sub-Poissonian statistics (anti-bunched photons). This property could be used to implement a single-photon switch [141], towards which much experimental progress has been realized [63, 142–144, 174, 175]. Also, photon correlation measurements could offer a technique to observe Jaynes-Cummings (JC) nonlinearities and transitions to higher order rungs of the JC ladder [176, 177]; nonlinearities that could be used to generate N–photon bundles [26, 178], where the photons released by the cavity system exist in well defined Fock states.

For the photon correlation measurements, the scanning laser is first tuned to the cavity resonance frequency and locked to a resonance of the 250 MHz free spectral range Fabry-Perot interferometer. The reflected and transmitted light is collected with a single-mode and multi-mode fiber, respectively, and is then detected with 'ID Quantique ID100-MM50' avalanche photodetectors (APD). Alternatively, we have performed a classical photon correlation measurement by using a fiber beam splitter (FBS) in reflection or transmission. The APDs have a timing jitter of about 100 ps,

but relatively small detection efficiencies of only $\sim 3\%$ at a wavelength of 940 nm. The signal from the two APDs is then analyzed using a 'Becker & Hickl SPC330' time-correlated single photon counter card. A neutral QD with a large cooperativity $C \approx 2.5$ was used in a polarization degenerate microcavity, the same QD–cavity system presented in Chapters 6 and 7. Typically light intensities of 1-10 pW were used to probe the QD-cavity system.

In Fig 9.1 we present preliminary results of photon correlation measurements. In Fig. 9.1 (a), signatures of the anti-bunching of light are shown, with $g^2(\Delta t = 0) \approx 0.5$. The input linear polarization was set to 45° with respect to the two fine split QD transitions and crossed polarizers were used to detect the reflected and transmitted light. A clear dip of coincidence events around $\Delta t = 0$ ns is visible.

On the other hand, we present a clear bunching feature in Fig. 9.1 (b), with $g^{(2)}(\Delta t = 0) \approx 2.4$. The polarization was set to match one of the fine split transitions, and the transmitted light was analyzed at the same polarization with a FBS. The bunching and anti-bunching signatures approximately correspond to Lorentzian functions (red curves) with a FWHM of 360 ps, which is approximately the convoluted timing resolution of two detectors. This indicates that the interaction of light and the coupled QD–cavity system occurs on a very fast timescale, probably on the order of the intra-cavity photon storage time $\tau \approx 1/2\kappa_m \approx 45$ ps.

To intuitively understand the photon correlation measurements, one could assume that if a n-photon Fock state interacts with the coupled QD–cavity system, one photon will have the transmittivity T_1 and reflectivity R_1 that corresponds to the coupled QD–cavity system (with cooperativity C), while the other $n-1$ photons will have transmittivity T_c and reflectivity R_c that corresponds to an empty system ($C = 0$). Photon anti-bunching then occurs in the general case when $T_1, R_1 > 0$ and $T_c, R_c = 0$. This is the case for example in Fig. 9.1 (a), where the photons that are not modified by the QD are eliminated by the crossed polarizer and any multi-photon state of light will be transformed into a single-photon state. This cross-polarized mode of operation could be of great interest for applications requiring a true single-photon source.

Photon bunching signatures on the other hand, are obtained in the general case when $T_1, R_1 < T_c, R_c$, as is for example shown in Fig. 9.1 (b). An initial Poisson distribution, with mean photon number $\overline{n}$ and standard deviation $\Delta n = \sqrt{\overline{n}}$, is now converted into a super–Poissonian state with $\overline{n}' < \overline{n}$ while the standard deviation $\Delta n' \approx \Delta n$ remains unchanged, and therefore $\Delta n'/\overline{n}' \approx \Delta n/\overline{n} > 1$. This implies that the bunching peak is strongly power dependent.

In reality, transitions to higher order rungs of the JC ladder, the excitation of the QD, and the fact that not every photon in the cavity interacts with the QD need to be considered as well, and the task of predicting photon correlations as function of input intensity, input and output polarizations, and QD-cavity detuning, becomes non-trivial. One approach could be to use numerical methods and solve the quantum master equation, such as provided by the Quantum Optics toolbox [40].

9.2 Cavity enhanced coupling with phonons

Electronic excitations in QDs can interact with their solid-state environment via phonons, which in principle is undesired as it decreases the coherence properties.

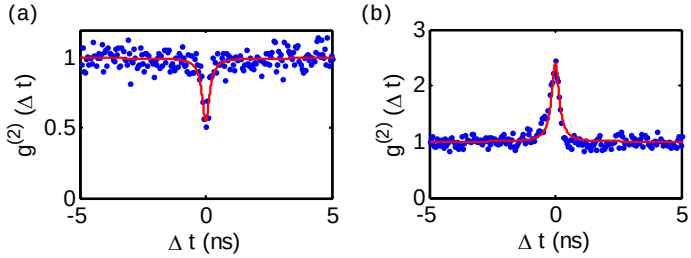

Figure 9.1: Photon time correlation measurements. (a) Anti-bunched signature, obtained at an in-coupling polarization $\theta_{in} = 45°$ while collecting reflected and transmitted light through crossed polarizers. (b) Bunched light, measured at $\theta_{in} = 0°$ while collecting the transmitted light at the same polarization.

Coupling to phonons is reduced however by the small $\sim$ 20 nm dimension of the QD, which prevents an interaction with phonons that have a larger wavelength, and by cooling down to cryogenic temperatures. Phonon–exciton coupling still occurs however and has been predicted theoretically [179], and observed experimentally [180, 181] in the form of Stokes and anti-Stokes features in the QD emission spectrum as a consequence of emission and absorption, respectively, of acoustic phonons. An asymmetry arises at low temperatures, as phonon absorption is suppressed while phonon emission still occurs.

Several theoretical proposals predict phonon–induced asymmetries to become enhanced in a coupled QD–cavity system [182, 183]. The general idea behind phonon induced dephasing is schematically depicted in Fig. 9.2. When a QD transition is detuned at the red-side of the cavity resonance and probed by a resonant laser, cavity enhanced absorption of a phonon and emission of a photon at the cavity resonance occurs, but is limited by the strong reduction of phonons at sufficiently low temperatures. A blue-detuned QD transition would experience a similar cavity-enhanced phonon induced decoherence, but then through the emission of a phonon. Unlike the red detuned case, here the decoherence process would persist even when there are initially no phonons present. This would result in an asymmetry in the QD lineshape: the faster dephasing rate at the blue-detuned side results in a broader QD feature and a smaller cooperativity.

Our system is in principle well suited to investigate such effects, as the QD-cavity detuning can be varied while keeping the temperature constant. Voltage tuning however brings the additional challenge that the QD experiences a voltage dependent dephasing rate. Within a certain voltage range or 'plateau', the charged state of the QD is well-defined, but at the edges of these plateaus fast additional co–tunneling or non-radiative decay processes of the exciton become dominant, which also gives rise to QD dephasing. It is therefore a challenge, for example in the experimental data presented in Fig. 9.2 where an asymmetry is clearly visible, to distinguish between the phonon effects and effects induced by the applied bias voltage.

One approach could be to strain-tune the QD while keeping the voltage constant, for example through the application of laser-induced surface defects which red-detune

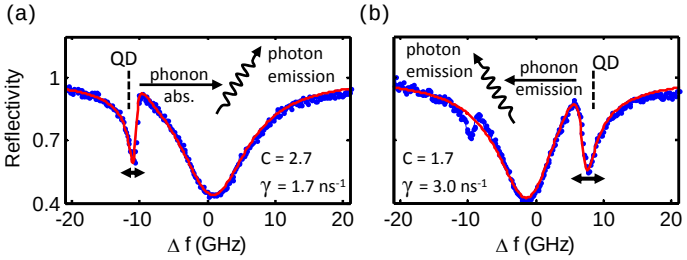

Figure 9.2: General idea behind phonon induced dephasing illustrated with measurements. (a) When a QD is red-detuned from the cavity resonance and is probed resonantly, cavity assisted absorption of a phonon and emission of a photon at the cavity frequency ($\Delta f = 0$ GHz) occurs, while for (b) a blue-detuned QD a similar process occurs but accompanied by phonon emission. At sufficiently low temperatures the phonon emission process (b) is more efficient, leading to an asymmetry in the QD dephasing rate γ.

the QD transitions [95]. Possibly it would also be beneficial to cool down to lower temperatures compared to the 9.0 K that is the current limit. As discussed in Chapter 2.1, hopefully the installation of additional temperature control of the cold head will make it possible to reach lower temperatures.

9.3 Using full polarization control for high fidelity spin–photon entanglement

In this section we will discuss some simulations on utilizing polarization control in a polarization degenerate microcavity. One of the long-term goals of this research project is to realize spin–photon entanglement by a scheme briefly discussed in Chapter 1.1. Such an experiment requires a singly charged QD with two ground states $|\uparrow\rangle$,$|\downarrow\rangle$, and the reflection or subsequent transmission of a photon depending on the spin state. The figures of merit for such a process to successfully occur could be defined as the ratio $R_\uparrow/R_\downarrow$ ($T_\downarrow/T_\uparrow$) of the spin-dependent reflectivity (transmittivity). Optimizing these ratios is also beneficial to observe spin quantum jumps [184–186], or to enhance the photon correlation features described in section 9.1. The figures of merit are however challenged by the non-unity in-coupling efficiency ($\eta \sim 0.3$ in our device) and the finite value of the QD cooperativity C. We will show that, by using a polarization degenerate cavity and clever tuning of the in- and out-coupling polarizations, these ratios can be greatly increased.

We consider a polarization degenerate cavity with a QD that has an energy level scheme as depicted in Fig. 9.3 (a). The QD is in an arbitrary superposition of the two ground states $|\Psi\rangle = \alpha|\uparrow\rangle + \beta|\downarrow\rangle$, with $|\alpha|^2 + |\beta|^2 = 1$. The general requirements for our polarization tuning scheme are that the two ground states couple to transitions of orthogonal polarization, and that there is a frequency splitting between the two levels. In the following, we simulate the case where there is a 2 GHz frequency splitting and the transitions couple to the same excited state and are linearly polarized (0° and 90°). This case could for example be achieved with a singly-charged QD and

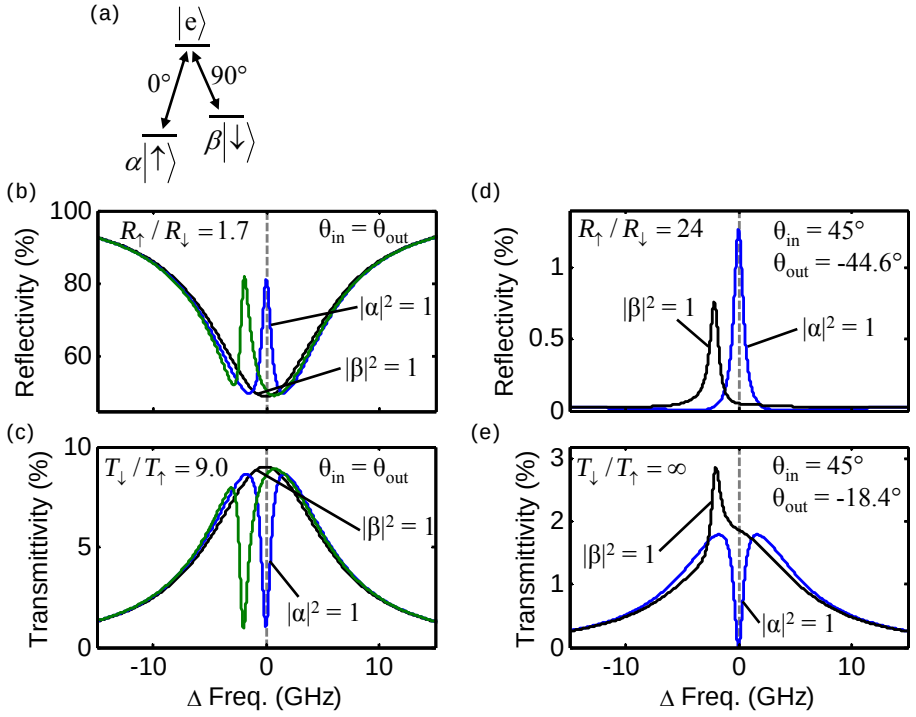

Figure 9.3: Demonstration of using detuned polarizers to increase the contrast of spin-dependent cavity reflection and transmission. (a) shows a schematic of the Zeeman split spin up/down ground states of a singly-charged QD that each couple with a linearly orthogonally polarized transition. The QD is in a superposition state $|\Psi\rangle = \alpha\,|\uparrow\rangle + \beta\,|\downarrow\rangle$. (b,c) Simulated reflectivity and transmittivity curves for the same input as output polarization. Blue curve: $\theta_{in} = 0°$ and $|\alpha|^2 = 1$, black curve: $\theta_{in} = 0°$ and $|\beta|^2 = 1$, green curve: $\theta_{in} = 90°$ and $|\beta|^2 = 1$. The fidelity is defined as the ratio between the blue and the black curve at the QD resonance indicated by the grey vertical dashed lines. (d,e) Simulated curves for $|\alpha|^2 = 1$ (blue) and $|\beta|^2 = 1$ (black), for input polarization $\theta_{in} = 45°$ and output polarization indicated in the figure window. For all the simulations $\eta = 0.3$, $\kappa = 77$ ns^{-1}, $C = 1$, $\gamma = 1$ ns^{-1} and frequency splitting of 2 GHz between the two spin states is used.

an in-plane magnetic field on the order of 1 T, see Chapter 2.3.5 and Figure 2.8 where we show this energy level scheme for a negatively charged QD. But an out-of-plane magnetic field configuration could also be used, where the ground states couple to corresponding excited states through circularly polarized transitions of different handedness and energy.

The two transitions, induced by linearly polarized light at 0° and 90°, correspond with transmission (reflection) amplitudes $t_\uparrow$ ($r_\uparrow = 1 - t_\uparrow$) and $t_\downarrow$ ($r_\downarrow = 1 - t_\downarrow$), an uncoupled cavity corresponds to transmission (reflection) amplitude t_c ($r_c = 1 - t_c$). Following methods described in Chapter 6, the transmittivity for $|\alpha|^2 = 1$ is given by $T_\uparrow = |\mathbf{e}_{out}^\dagger \begin{pmatrix} t_\uparrow & 0 \\ 0 & t_c \end{pmatrix} \mathbf{e}_{in}|^2$, while $T_\downarrow = |\mathbf{e}_{out}^\dagger \begin{pmatrix} t_c & 0 \\ 0 & t_\downarrow \end{pmatrix} \mathbf{e}_{in}|^2$ for $|\beta|^2 = 1$. Here, $\boldsymbol{e_i} = (cos(\theta_i), sin(\theta_i))$ defines the linear input/output (i =in/out) polarization with angle θ_i.

We consider a cavity with $\eta = 0.3$ and $\kappa = 77$ ns^{-1}, similar to the one studied throughout this thesis. For the QD we use $C = 1$, $\gamma = 1$ ns^{-1}, and a splitting of 2 GHz between the two transitions. Figure 9.3 (b,c) shows the reflectivity and transmittivity for the case where $\mathbf{e}_{in} = \mathbf{e}_{out}$. The blue curve shows the case for $\theta_{in} = 0°$ and $|\alpha|^2 = 1$, and the black curve shows the case for the same incoming polarization but $|\beta|^2 = 1$. The ratios between these two curves at the resonance frequency (laser-cavity detuning $\Delta f = 0$ GHz) of the spin-up transition are shown in the figure panels. The green curve shows as a reference the case for $\theta_{in} = 90°$ and $|\beta|^2 = 1$.

Figure 9.3 (d,e) shows that the fidelities can be dramatically increased by using an input polarization $\theta_{in} = 45°$ and detuning the output polarization. This does come at the expense of a reduced throughput of light through the system. In order to achieve larger fidelities and reduce losses, the in-coupling efficiency η and QD cooperativity C will have to be further increased.

9.4 Further sample improvements

All experiments described in Chapters 5-8 were performed with samples fabricated from the '131018A' wafer. There are however three shortcomings of this wafer: (i) the singly-charged QD suffers from fast decoherence, (ii) the incoupling efficiency is limited to $\eta = 0.3$, and (iii) it could be more advantageous to switch from negatively charged QDs to positively charged ones. In the following subsections we will discuss these shortcomings and propose sample improvements.

9.4.1 Charged QD decoherence

The main drawback of the samples produced from the '131018A' wafer material is that the singly-charged QDs suffer from fast decoherence. We conclude this from three observations: (i) in Chapter 6 we measured dephasing rates $\gamma \sim 9$ ns^{-1} that are a factor 20 larger than expected from the measured radiative lifetime of 1.2 ns, (ii) the crossed polarization signal shown in Fig. 6.4 (e) is too large to be explained by a 'coherent' model and seems to indicate that linear light is instantaneously projected onto a circular basis by the QD interaction (the 'incoherent' model), and (iii) the interference technique measurements shown in Fig. 8.3 in Chapter 8 demonstrate a nearly complete incoherent scattered signal. This dephasing is a limitation for using

a single charge as a spin qubit, and in general makes experiments challenging as the cooperativity $C = g^2/\kappa\gamma$ is, as we have found so far, limited to values of $C < 0.3$, to be compared to the maximum value $C = 2.5$ we found for a charge neutral QD.

We hypothesize that a fast co-tunneling process lies at the heart of this, and one thing to investigate would be to increase the tunnel barrier from 20 nm to 35 nm for a negatively charged QD sample, as was used in previous work were a QD spin-state was prepared with near-unity fidelity [107]. For future positively charged QD samples a tunnel barrier of 25 nm should be sufficient, since heavy holes have a larger effective mass compared to electrons, and this tunnel barrier thickness was used to demonstrate optical pumping of a hole spin [187],

9.4.2 In-coupling efficiency

Another drawback is the non-unity in-coupling efficiency $\eta = 2\kappa_m/(2\kappa_m + \kappa_s) \approx 0.3$. One approach to improve η is to decrease the absorption/scattering loss rate $\kappa_s \approx 5\kappa_m \approx 55$ ns^{-1} in the current sample. We hypothesize that κ_s is limited by absorption by the doped layers, and can be decreased by reducing the doping concentrations. Another approach would be to increase the mirror loss rate κ_m by using less Bragg pairs in the mirrors, but this comes at the cost of a reduced cavity Q–factor.

9.4.3 Switch from electron spins to hole spins

A final improvement would be to switch from negatively charged QDs to positively charged ones. Electron spins experience hyperfine interaction with nuclear spins which limits their coherence time. Hole spins have p-orbitals, and partially d-orbitals, and therefore experience only about 10% of the hyperfine interaction compared to electrons [188–190]. They do experience dipole-dipole coupling but this only acts in the out-of-plane growth direction, and by applying an in-plane magnetic field this effect can be canceled [191]. Several experiments have indeed demonstrated coherent properties of hole spins and promising coherence times of at least $T_2 > 100$ ns [106, 192].

An additional, but less significant, benefit of switching to hole spins, is that hole spins have a smaller in-plane g-factor compared to electron spins $|g_h| < |g_e|$ [108, 192]. The Zeeman splitting $\Delta E_h = g_{h,e}\mu_B B_x$ of the ground state is therefore smaller compared to the splitting of the excited states, which make the transitions from the ground states to the lowest energy excited state lower in energy compared to the transitions to the second excited state. This way a Λ-system is realized that is energetically separated from other unwanted transitions. This could be of interest in order to use such techniques as presented in Refs. [193, 194], where an arbitrary ground state superposition is obtained by directly mapping the polarization of an incoming light pulse onto the spin state, through a technique related to coherent population trapping.